Relative humidity gradients as a key constraint on terrestrial water and energy fluxes

Authors: Yeonuk Kim[1,*], Monica Garcia[2], Laura Morillas[3], Ulrich Weber[4], T. Andrew Black[5], Mark S. Johnson[1,3,6]

Affiliations:

[1]*Institute for Resources, Environment and Sustainability, University of British Columbia, Vancouver, V6T1Z4, Canada.*

[2]*Department of Environmental Engineering, Technical University of Denmark, Lyngby, 2800, Denmark.*

[3]*Center for Sustainable Food Systems, University of British Columbia, Vancouver, V6T1Z4, Canada.*

[4]*Max Planck Institute for Biogeochemistry, Hans Knoell Strasse 10, 07745 Jena, Germany*

[5]*Faculty of Land and Food Systems, University of British Columbia, Vancouver, V6T1Z4, Canada.*

[6]*Department of Earth, Ocean and Atmospheric Sciences, University of British Columbia, Vancouver, V6T1Z4, Canada.*

*Correspondence to: yeonuk.kim.may@gmail.com

Abstract:

Earth's climate and water cycle are highly dependent on the latent heat flux (*LE*) associated with terrestrial evapotranspiration. While the widely-used Penman-Monteith *LE* model is useful to explore vegetative controls on *LE*, land-atmosphere interactions are difficult to interpret due to the complex role of biological controls on underlying physical processes. Here, we present a novel *LE* model that defines *LE* as a combination of diabatic (heat-driven) and adiabatic (relative humidity (*rh*) gradient-driven) processes using only abiotic variables. This approach yields new insights on the fundamental characteristics of *LE*. Here we show that the ratio of *LE* to available energy is mainly controlled by vertical *rh* gradients, but the spatiotemporal variability in *rh* gradients are small due to equilibration at the land-atmosphere boundary. Consequently, the global mean vertical *rh* gradient is near zero, implying land-atmosphere equilibrium at the global-scale. As a result, the spatiotemporal variability of *LE* is largely determined by the diabatic term, which can be readily determined by standard meteorological measurements. Our proposed model and findings provide a fundamental benchmark for *LE* predictions. By demonstrating how land surface conditions become encoded in the atmospheric state, our model will also help to improve our understanding of Earth's climate system and water cycle.

Main text:

Latent heat flux (*LE*) associated with plant transpiration and evaporation from soil and intercepted water is the key component linking the water cycle and the terrestrial energy budget. More than half of the incoming radiation energy at the land surface is consumed as *LE*, making evapotranspiration (i.e., the sum of evaporation and transpiration) the second largest flux in the terrestrial water balance after precipitation [1], and a key driver of Earth's climate system [2]. However, because the land surface is heterogeneous and mainly unsaturated, our ability to predict *LE* remains inadequate, as evidenced by poorly constrained representations of *LE* in the current generation of climate models [3]. While most research has been devoted to developing and improving rate-limiting parameters constraining *LE* such as García, et al. [4], exploring the governing physics of *LE* has received less attention following earlier pioneering work [5-8]. Understanding the governing physics is especially important in the era of the Anthropocene since the variability of *LE* has become more unpredictable [9,10].

A traditional way to understand the governing physics is to partition *LE* into diabatic and adiabatic processes using the Penman-Monteith (PM) equation [7], as proposed by Monteith [11]. The PM equation combines the energy balance equation with mass-transfer theory for water vapour and sensible heat, resulting in diabatic (radiative energy-related) and adiabatic (vapour pressure deficit-related) processes for a parcel of air in contact with a saturated surface [11].

$$LE = \underbrace{\frac{S}{S+\gamma(\frac{r_a+r_s}{r_a})} \cdot Q}_{Diabatic\ process} + \underbrace{\frac{\rho c_p}{S+\gamma(\frac{r_a+r_s}{r_a})} \cdot \frac{e^*(T_a)-e_a}{r_a}}_{Adiabatic\ process} \quad (1)$$

where S is the linearized slope of saturation vapour pressure versus temperature (hPa K^{-1}), γ is the psychrometric constant (hPa K^{-1}), ρ is the air density (kg m^{-3}), c_p is the specific heat capacity of air at constant pressure (MJ kg^{-1} K^{-1}), and Q is available radiative energy (i.e., difference between net radiation and soil heat flux and expressed in units of W m^{-2}). $e^*(T_a)$ is the saturation vapour pressure (hPa) at air temperature (T_a) measured at a reference height, and e_a is vapour pressure (hPa) at the reference height. The term [$e^*(T_a)$- e_a] is known as atmospheric vapour pressure deficit (VPD, expressed in units of hPa). r_a is total aerodynamic resistance to heat and water vapour transfer (s m^{-1}), and r_s is surface resistance to water vapour transfer (s m^{-1}) representing drying soil and/or plant stomatal closure.

In principle, high VPD at the reference height increases the adiabatic term in Eq. (1) [12]. Yet, this "high VPD leads to high *LE*" interpretation cannot be generalized because r_s increases with VPD due to stomatal closure by vegetation under high VPD conditions [13-15]. While the PM equation is useful to explore biological control of *LE* through r_s [5], physical mechanisms of each term in Eq. (1) are less intuitive due to the sensitivity of r_s to VPD.

Is there a way to mathematically express the physical mechanisms of *LE* without requiring r_s? Helpfully, Monteith [11] provided another form of the *LE* model for the case when the surface does not reach saturation (i.e., the relative humidity (*rh*) of the surface is less than unity), and for which r_s is not required. Here, we further find that there are two mathematical expressions of *LE* which are capable of accounting for the vertical gradients in *rh*. The following pair of equations allow us to capture the thermodynamic process governing turbulent heat exchange between the land surface and the atmosphere, including under unsaturated land surface conditions (derivation in Appendix A).

$$LE = \underbrace{\frac{rh_s S}{rh_s S+\gamma} \cdot Q}_{Diabatic\ process:\ LE_Q} + \underbrace{\frac{\rho c_p e^*(T_a)}{rh_s S+\gamma} \cdot \frac{rh_s - rh_a}{r_a}}_{Adiabatic\ process:\ LE_G} = LE_Q + LE_G \tag{2}$$

$$LE = \underbrace{\frac{rh_a S}{rh_a S+\gamma} \cdot Q}_{Diabatic\ process:\ LE_Q{'}} + \underbrace{\frac{\rho c_p e^*(T_s)}{rh_a S+\gamma} \cdot \frac{rh_s - rh_a}{r_a}}_{Adiabatic\ process:\ LE_G{'}} = LE_Q{'} + LE_G{'} \tag{3}$$

where rh_s and rh_a are rh at the land surface and the reference height, respectively. Equations (2) and (3) include rh_s to compensate for eliminating r_s from the original PM equation. Since the adiabatic process in Eqs. (2) and (3) are controlled by the vertical difference of rh, we refer to Eqs. (2) and (3) as the proposed PM_{rh} model (Penman-Monteith equation expressed using rh) to distinguish it from the original PM model. The two equations represent different thermodynamic paths which will be discussed in the next section. Arguably, applying PM_{rh} can provide new insights into the fundamental mechanisms of LE, particularly when it is decomposed into its energy driven diabatic component (LE_Q or $LE_Q{'}$) and its adiabatic component (LE_G or $LE_G{'}$) that is driven by the gradient in rh.

In this paper, we first present the theory of our PM_{rh} model, and apply it empirically to an eddy-covariance observation site. Also, the proportion of net available energy consumed in evapotranspiration, known as the evaporative fraction ($EF = \frac{LE}{Q}$) is decomposed into $\frac{LE_Q}{Q}$ and $\frac{LE_G}{Q}$. Finally, we apply the decomposition approach to a global LE dataset [16] to understand how LE_Q and LE_G vary spatiotemporally in different regions of the world, and discuss how these patterns can help to understand land-atmosphere interactions and potential responses under future climatic conditions.

Theory and observational evidence.

Before discussing PM_{rh} in-depth, we revisit the Penman equation [6] to help with the physical reasoning behind our proposed framework. The widely recognized form of the Penman equation, which was developed as an *LE* model for a saturated surface, is as follows:

$$LE = \underbrace{\frac{S}{S+\gamma} \cdot Q}_{Diabatic\ process} + \underbrace{\frac{\rho c_p [e^*(T_a) - e_a]}{[S+\gamma] r_a}}_{Adiabatic\ process} \tag{4}$$

We rearrange this original formulation to derive Eq. (5) by factoring out $e^*(T_a)$ and introducing $rh_a = \frac{e_a}{e^*(T_a)}$ into the second term.

$$LE = \underbrace{\frac{S}{S+\gamma} \cdot Q}_{Diabatic\ process} + \underbrace{\frac{\rho c_p e^*(T_a)}{S+\gamma} \cdot \frac{1-rh_a}{r_a}}_{Adiabatic\ process} \tag{5}$$

Equations (4) and (5) are mathematically equivalent, but their interpretations are quite different. In Eq. (4), the adiabatic process is controlled by VPD at the reference height. However, in Eq. (5), the adiabatic process acts over the vertical *rh* difference from the surface to the reference height. Since the Penman equation is a model for saturated surfaces, $1 - rh_a$ in Eq. (5) indicates the vertical *rh* difference. Arguably, Eq. (5) is more thermodynamically sound compared to Eq. (4) since *rh* is an ideal-gas approximation to the water activity [17] which represents the chemical potential of water (μ_w) [12,18]. When the vertical gradient of *rh* dissipates, the land surface and the atmosphere are in thermodynamic equilibrium [19]. Therefore, taking Eq. (5) instead of Eq. (4) allows us to view the adiabatic process of the Penman model as a reequilibration process driving land-atmosphere equilibrium by bringing the surface μ_w to that of the atmosphere.

As with our interpretation of the Penman model, we can view Eq. (2), as a generalized form of the Penman model. Here, the LE_G $(= \frac{\rho c_p e^*(T_a)}{rh_s S+\gamma}\frac{rh_s - rh_a}{r_a})$ term of Eq. (2) is an reequilibration process between the land and the atmosphere when the land surface is not saturated. It is worth noting that LE_G can be negative when rh_s is less than rh_a. Thus, the LE_G term acts to reduce the vertical *rh* gradient. This physical interpretation is consistent with recent findings that the variance of the *rh* gradient tends to be minimized over the course of the day [20,21]. The diabatic LE_Q $(= \frac{rh_s S}{rh_s S+\gamma} Q)$ term can be understood as equilibrium *LE* for an unsaturated surface as was recently suggested by McColl, et al. [22], which we discuss later in this section.

How then can we interpret the two formulas of PM_{rh} in Eqs. (2) and (3)? To explain the two forms, we use the psychrometric relationship applied to a parcel of air near an unsaturated land surface that is under constant pressure and steadily receiving radiation energy [11]. The initial thermodynamic state of the air parcel can be represented by its temperature and water vapour pressure such as point A in Figure 1. The initial state is changed by two processes as follows: (1) equilibrating between the land surface (rh_s) and the air parcel (rh_a), and (2) increasing enthalpy forced by the incoming energy.

In the equilibrating process, the air parcel is adiabatically cooled (or heated when rh_s < rh_a), while the enthalpy of the parcel is not changed. Therefore, the increase (decrease) in latent heat content in the parcel is exactly balanced by a decrease (increase) in sensible heat ($A \rightarrow B$ in Figure 1: trajectory along constant enthalpy line). This process is equivalent to the LE_G term in Eq. (2). Now, the air parcel is in thermodynamic equilibrium with the land surface (point B in

Figure 1). Then, the air parcel receives energy while the equilibrium is sustained (i.e., rh_s is steady), which increases both the temperature and absolute water vapour content of the air parcel ($B \rightarrow C$ in Figure 1). This process can be expressed as LE_Q of Eq. (2). Consequently, the thermodynamic state of the air parcel approaches point C in Figure 1.

However, we should recognize that temperature and vapour pressure are “state” variables meaning that they do not depend on the thermodynamic path by which the system arrived at its final state [23]. In the above example, we conceptually followed the adiabatic process first and then the diabatic process (Path 1 in Figure 1), but one can imagine the opposite order. If we choose Path 2 in Figure 1, the diabatic process comes the first, and thus rh_a instead of rh_s is preserved while enthalpy increases (i.e., LE_Q'), and the adiabatic process is followed at temperature of T_S (i.e., LE_G'). Path 2 is described by Eq. (3).

Therefore, one can interpret the two forms of PM_{rh} in Eqs. (2) and (3) as two thermodynamic paths where the diabatic and adiabatic processes occur simultaneously. It should be noted that the diabatic and adiabatic processes in PM_{rh} are “path” functions and thus they vary by path. For instance, LE_Q is slightly higher than LE_Q' when $rh_s > rh_a$. However, as shown by Figure 2 (a1) and (a2), observational data from around the world represented in the FLUXNET2015[24] dataset indicate that differences between LE_Q and LE_Q', as well as differences between LE_G and LE_G', are marginal at daily time scale. This is an important point since LE_Q' can be determined simply and directly using by reference height meteorological measurements, while LE_Q is required to know rh_s.

Another distinct characteristic of the PM_{rh} model is the way it defines equilibrium at the land-atmosphere interface. Unlike many previous studies which focused on the vertical gradient of VPD [8,25,26], land-atmosphere equilibrium is achieved in the PM_{rh} model when the vertical *rh* gradient (i.e., the μ_w gradient) dissipates. That is, if $rh_s \approx rh_a$, then it follows that LE_G (or LE_G') is zero and thus LE becomes

$$LE \approx \frac{rh_a S}{rh_a S + \gamma} Q \tag{6}$$

Equation (6), is identical to the "surface flux equilibrium (SFE)" theory recently introduced by McColl, et al. [22]. They hypothesized that in many continental regions, the near surface atmosphere is in state of SFE, where the surface moistening and surface heating terms are balanced in the *rh* budget, especially at longer time scales. Equation (6) successfully predicted observed *LE* at daily and multiday time scales for inland regions [27], which implies the vertical *rh* gradient tends to zero. This is logical in that LE_G itself operates to diminish the vertical *rh* gradient. Our analysis in Figure 2 also indicates that the mean value of daily LE_G of all FLUXNET2015 sites is close to zero, implying global-scale land-atmosphere equilibrium. Importantly, *LE* is primarily determined by LE_Q (R^2 = 0.65) instead of LE_G (R^2 = 0.18). Nevertheless, FLUXNET2015 data suggests that LE_G is the main driver of local-scale variability of EF at the daily time scale (Figure 2 (c1) and (c2)).

Time series of decomposed *LE*.

In order to explore the influence of varying conditions on individual decomposed *LE* terms and identify land-atmosphere equilibrium conditions, we applied the PM_{rh} model to multi-year observational eddy-covariance data collected at an irrigated sugarcane farm in Costa Rica. The site has wet-dry tropical climate with a dry season from December to March. The decomposition analysis of LE shows that while LE_Q is the major component of LE, LE_G variability plays a major role in seasonal behavior of LE, which is confirmed by wavelet analysis (Fig. 3 d1-d2). Interestingly, the annual mean LE_G was the highest in 2015, a drought year in which rh_a was generally lower than for the other years, while the annual mean LE_G was close to zero only in 2016 when there was no application of dry season irrigation.

To explore the diurnal behaviour of decomposed LE, we selected different surficial and atmospheric conditions when LE_G was zero, positive, or negative in Fig. 3 (c1) - (c4). In the 2016 dry season, LE_G was close to zero as a daily average value, as a result of negative daytime and positive nighttime LE_G values due to dry air and dry soil conditions (no irrigation) and undeveloped vegetation canopy (Fig. 3 (c1)). Daily LE_G was also close to zero during wet season conditions (e.g., Fig. 3 (c2)). In this case, LE_G was near zero during both daytime and nighttime periods due to near saturated atmospheric and land surface conditions. These two cases show that dry land-dry air or wet land-wet air conditions can each lead to daily scale land-atmosphere equilibrium (i.e., $LE_G \approx 0$), although the diurnal pattern of LE_G is starkly different for dry land-dry air vs. wet land-wet air conditions.

Meanwhile, when rh_a was low (≈0.55) and the canopy was well-developed, LE_G was found to be positive during both daytime and nighttime periods (Fig. 3 (c3)). On the other hand, during post-harvest conditions when vegetative canopy cover was minimal and air and soil moisture levels were low, daily LE_G was found to be negative as a result of negative daytime and positive nighttime LE_G values (Fig. 3 (c4)). Regarding the overall diurnal pattern, LE_G generally declined during the morning and increased in the afternoon, which is consistent with the well-known diurnal pattern of EF [28,29] (Fig. 3 (c5)).

Spatial pattern of decomposed *LE*.

We then applied the PM_{rh} model to the FLUXCOM dataset, a benchmark global *LE* data product [16]. As shown in Fig 4 (a) and (c), the spatial patterns of the annual mean *LE* and LE_Q were similar. The monthly time series of global *LE* and its two components in Fig 4 (e1) show that LE_G is consistently close to zero and that *LE* is mostly determined by LE_Q (R^2 = 0.85) instead of LE_G (R^2 = 0.18) (Fig 4 (f1) and (f2)). This result is consistent with Eq. (6) and the SFE theory. In other words, the land surface is generally under thermodynamic equilibrium with the atmosphere at the global-annual scale (i.e., $rh_s \approx rh_a$).

However, while mean annual LE_G was close to zero in broad areas (particularly in high latitude regions), it was distinctly positive or negative in many regions (Fig 4 (d)). In humid tropical regions like the Amazon basin where moisture convergence is large, LE_G was generally positive, whereas arid regions such as Australia where characterized by negative LE_G (Fig 4 (e3) and (e4)). The spatial pattern of LE_G is similar to the spatial pattern of EF (Fig 4 (b)). The finding that that the spatial variation of EF is primarily controlled by LE_G instead of LE_Q was supported by correlation analyses (R^2 = 0.60 for EF~LE_G and R^2 = 0.28 for EF~LE_Q; Fig 4 (f3) and (f4)).

Discussion.

As described in the theory section, land-atmosphere equilibrium is achieved when LE_G approaches zero and thus *LE* reduces to Eq. (6). The decomposed terms derived from both the empirical FLUXNET and model-based FLUXCOM datasets show that the global mean for LE_G is near zero, implying global-scale land-atmosphere equilibrium (Fig 2 and Fig 4). This result extends the SFE theory of McColl, et al. [22]. Although, LE_G is not always near zero particularly in low latitude regions where the influence of the ocean and atmospheric on rh_a is significant[30], moisture convergence and divergence at the global-scale tend to balance each other, out resulting global-scale land-atmosphere equilibrium. Moisture convergence and divergence drives spatiotemporal variability of EF at local scales, with moisture convergence vs. divergence appearing encoded as the sign of LE_G. Indeed, the spatial pattern in Fig 4 (d) clearly distinguishes atmospheric moisture convergence regions such as South Atlantic convergence zone (SACZ) of southeastern Brazil (25°S, 55°W).

Salvucci and Gentine [20] found that the variance of the *rh* gradient tends to be minimized over the course of the day, and they developed an approach to predict *LE* based on this finding. However, its physical mechanisms remain elusive. Our PM_{rh} model provides theoretical support for Salvucci and Gentine's approach [20] in that LE_G acts to reduce the *rh* gradient. Indeed, the diurnal cycles of the LE_G in Fig 3 are aligned with their findings with respect to the sign of LE_G during daytime and nighttime. Over the course of the day, rh_a coevolves with rh_s through the equilibration process (i.e., LE_G), and thus the land surface moisture status is linked to rh_a. This interpretation also can explain the widely-accepted Bouchet's complementary hypothesis[31] in that land wetness can be parameterized based on rh_a such as Priestley-Taylor (PT) JPL *LE* prediction model [4,32].

In summary, we have shown that our novel PM_{rh} model provides a new opportunity to understand the governing physics of the terrestrial energy budget. Our findings suggest that while LE_G is a primary component determining EF, spatiotemporal variability of LE_Q alone can adequately represent the variability of *LE*. Our analyses reveal global-scale land-atmosphere equilibrium which can be a fundamental benchmark against which *LE* predictions derived from climate models can be assessed. Also, our analysis shows how the land surface conditions become encoded to the atmospheric state. Questions remain regarding how LE_Q and LE_G will be influenced in relation to changing climatic and land surface conditions, and how these changes might affect the climate system at differing spatial and temporal scales through positive or negative feedbacks.

Methods.

<u>FLUXNET2015.</u> The daily scale FLUXNET2015 dataset, which includes 212 empirical eddy-covariance flux tower sites around globe, was used in this study [24]. The turbulent heat fluxes, net radiation, soil heat flux, air temperature, relative humidity, wind speed, friction velocity, and barometric pressure were obtained from the dataset and then quality-controlled (details in Appendix B). In order to decompose daily LE into LE_Q and LE_G, we first estimated daily aerodynamic resistance (r_a) by considering aerodynamic resistance to momentum transfer and the additional boundary layer resistance for heat and mass transfer (or excess resistance) [12,33,34].

$$r_a = \frac{u_*^2}{u(z_r)} + 6.2u_*^{-0.67} \quad (7)$$

The first term on the right hand side of Eq. (7) is the aerodynamic component and the second term is the boundary layer component. Here, u_* is friction velocity and $u(z_r)$ is reference height wind speed. r_a was estimated using the bigleaf R package [33].

By rearranging Eq. (2), rh_s can be calculated using.

$$rh_s = \frac{\gamma LEr_a/\rho c_p + e_a}{SHr_a/\rho c_p + e^*(T_a)} \quad (8)$$

LE_Q and LE_Q' were calculated using rh_a and rh_s following Eqs. (2) and (3), and then LE_G and LE_G' were calculated by subtracting LE_Q and LE_Q' from LE. To calculate LE_Q and LE_Q', we define Q as $LE + H$, but it should be noted this approach can include systematic uncertainty since the sum of LE and H measured by eddy-covariance system is typically lower than the difference between net radiation (R_n) and the soil heat flux (G) (i.e., conditions referred to as the energy balance closure problem [35]). To investigate the effect of energy balance closure problem, we provide Figure S1 that was generated by 1) defining Q as R_n-G, and 2) correcting LE and H based on the assumption that the Bowen ratio ($B = H/LE$) is correct [24]. We found that Figure S1 and Figure 2 are almost identical, implying that the lack of surface energy balance closure does not significantly impact our analyses and interpretations.

<u>In-situ dataset.</u> In-situ half-hourly eddy-covariance observations used in this study were made from 2015 to 2018 on a ratoon sugarcane farm in the province of Guanacaste, Costa Rica (10°25′07.60″N; 85°28′22.22″W). The site has a wet-dry tropical climate with a dry season from December to March and a median monthly air temperature ranging from 27 °C to 30 °C. The study site experienced drought in 2015 [36]. The site was irrigated occasionally during dry seasons via furrow irrigation events, except for 2016 when there was no irrigation due to crop replanting. Due to ratooning practice (detailed explanation in Appendix B), the sugarcane growing seasons varied by year, which provided an opportunity to explore distinct and varied combinations of land cover fraction and atmospheric aridity conditions.

The measurement data were quality controlled following Morillas, et al. [36] (details in Appendix B). Half-hourly r_a was then estimated by Eq. (9) instead of Eq. (7) in order to explicitly include atmospheric stability and canopy height dynamics [33].

$$r_a = \frac{ln[\frac{z_r - d}{z_{0m}}] - \psi_h}{k u_*} + 6.2 u_*^{-0.67} \qquad (9)$$

where, k is the von Kármán constant (0.41), d is the zero-plane displacement height ($d = 0.7z_h$), z_{0m} is the roughness length for momentum ($z_{0m} = 0.1z_h$), ψ_h is the integrated form of the stability correction function. z_h is canopy height based on manual measurements taken during regular maintenance visits. r_a was estimated using bigleaf R package [33] and rh_s was calculated from Eq. (8). Negative H and inaccurate r_a modelling sometimes yielded negative rh_s or values greater than one, especially at nighttime. In these cases, rh_s was assigned the value of one following the approach described in the bigleaf R package [33]. We then estimated LE_Q and LE_G from Eq. (2).

FLUXCOM *LE* dataset decomposition. The FLUXCOM dataset [16] is a global-scale machine learning ensemble product which upscales FLUXNET observations [37] using Moderate Resolution Imaging Spectroradiometer (MODIS) satellite data and reanalysis meteorological data. In this study we used the monthly *LE* dataset (0.5° resolution) modelled using MODIS and ECMWF ERA5 reanalysis data.

From our analyses of the FLUXNET2015 global empirical data we learned that LE_Q and LE_Q' are almost identical. Therefore, instead of trying to model LE_Q, we simply estimated LE_Q as LE_Q'. Here, Q was obtained from the FLUXCOM output, and air temperature and relative humidity were retrieved from ERA5-Land monthly averaged data (2 m height). LE_G was then estimated by subtracting LE_Q from LE.

Acknowledgments: We want to thank Dr. Iain Hawthorne, Pável Bautista, Silja Hund, Cameron Webster, Gretel Rojas Hernandez, Guillermo Duran Sanabria, Dr. Andrea Suarez Serrano, Dr. Ana Maria Duran, Martin Martinez, and Dr. Fermin Subrios Ruiz for field and logistical support. We also thank Dr. Martin Jung, the principal investigator of the FLUXCOM dataset. The authors would like to thank the EU and NSERC for funding in the frame of the collaborative international Consortium AgWIT financed under the ERA-NET WaterWorks2015 Cofunded Call. This ERA-NET is an integral part of the 2016 Joint Activities developed by the Water Challenges for a Changing World Joint Programme Initiative (Water JPI).

Author contributions: Y.K. and M.S.J. designed research; U.W. provided FLUXCOM data; Y.K., L.M., and M.S.J. performed research; Y.K. analyzed data; Y.K., M.G., L.M., T.A.B, and M.S.J. wrote the paper.

Competing interests: Authors declare no competing interests.

References:

1 Oki, T. & Kanae, S. Global hydrological cycles and world water resources. *Science* **313**, 1068-1072 (2006).

2 Willett, K. *et al.* HadISDH land surface multi-variable humidity and temperature record for climate monitoring. *Climate of the Past* **10** (2014).

3 Ma, H.-Y. *et al.* CAUSES: On the Role of Surface Energy Budget Errors to the Warm Surface Air Temperature Error Over the Central United States. *Journal of Geophysical Research: Atmospheres* **123**, 2888-2909, doi:10.1002/2017jd027194 (2018).

4 García, M. *et al.* Actual evapotranspiration in drylands derived from in-situ and satellite data: Assessing biophysical constraints. *Remote Sensing of Environment* **131**, 103-118, doi:10.1016/j.rse.2012.12.016 (2013).

5 Jarvis, P. G. & McNaughton, K. G. in *Advances in ecological research* Vol. 15 1-49 (Elsevier, 1986).

6 Penman, H. L. Natural evaporation from open water, bare soil and grass. *Proceedings of the Royal Society of London. Series A. Mathematical and Physical Sciences* **193**, 120-145 (1948).

7 Monteith, J. L. in *Symposia of the society for experimental biology.* 205-234 (Cambridge University Press (CUP) Cambridge).

8 Priestley, C. H. B. & Taylor, R. J. On the Assessment of Surface Heat Flux and Evaporation Using Large-Scale Parameters. *Monthly Weather Review* **100**, 81-92, doi:10.1175/1520-0493(1972)100<0081:otaosh>2.3.co;2 (1972).

9 Milly, P. C. D. *et al.* Stationarity Is Dead: Whither Water Management? *Science* **319**, 573-574, doi:10.1126/science.1151915 (2008).

10 Marvel, K. *et al.* Twentieth-century hydroclimate changes consistent with human influence. *Nature* **569**, 59-65, doi:10.1038/s41586-019-1149-8 (2019).

11 Monteith, J. L. Evaporation and surface temperature. *Quarterly Journal of the Royal Meteorological Society* **107**, 1-27, doi:10.1002/qj.49710745102 (1981).

12 Monteith, J. & Unsworth, M. *Principles of environmental physics: plants, animals, and the atmosphere*. (Academic Press, 2013).

13 Novick, K. A. *et al.* The increasing importance of atmospheric demand for ecosystem water and carbon fluxes. *Nat Clim Change* **6**, 1023, doi:10.1038/nclimate3114 (2016).

14 Tan, C. S., Black, T. A. & Nnyamah, J. U. A Simple Diffusion Model of Transpiration Applied to a Thinned Douglas-Fir Stand. *Ecology* **59**, 1221-1229, doi:10.2307/1938235 (1978).

15 Massmann, A., Gentine, P. & Lin, C. When Does Vapor Pressure Deficit Drive or Reduce Evapotranspiration? *Journal of Advances in Modeling Earth Systems* **11**, 3305-3320, doi:10.1029/2019ms001790 (2019).

16 Jung, M. *et al.* The FLUXCOM ensemble of global land-atmosphere energy fluxes. *Scientific Data* **6**, 74, doi:10.1038/s41597-019-0076-8 (2019).

17 Lovell-Smith, J. W. *et al.* Metrological challenges for measurements of key climatological observables. Part 4: atmospheric relative humidity. *Metrologia* **53**, R40-R59, doi:10.1088/0026-1394/53/1/r40 (2015).

18 Kleidon, A. & Schymanski, S. Thermodynamics and optimality of the water budget on land: A review. *Geophysical Research Letters* **35**, doi:10.1029/2008gl035393 (2008).

19 Kleidon, A., Schymanski, S. & Stieglitz, M. in *Bioclimatology and Natural Hazards* (eds Katarína Střelcová *et al.*) 107-118 (Springer Netherlands, 2009).

20 Salvucci, G. D. & Gentine, P. Emergent relation between surface vapor conductance and relative humidity profiles yields evaporation rates from weather data. *Proceedings of the National Academy of Sciences* **110**, 6287-6291, doi:10.1073/pnas.1215844110 (2013).

21 Rigden, A. J. & Salvucci, G. D. Evapotranspiration based on equilibrated relative humidity (ETRHEQ): Evaluation over the continental U.S. *Water Resources Research* **51**, 2951-2973, doi:10.1002/2014wr016072 (2015).

22 McColl, K. A., Salvucci, G. D. & Gentine, P. Surface Flux Equilibrium Theory Explains an Empirical Estimate of Water-Limited Daily Evapotranspiration. *Journal of Advances in Modeling Earth Systems* **0**, doi:10.1029/2019ms001685 (2019).

23 Iribarne, J. V. & Godson, W. L. *Atmospheric thermodynamics*. Vol. 6 (Springer Science & Business Media, 2012).

24 Pastorello, G. *et al.* The FLUXNET2015 dataset and the ONEFlux processing pipeline for eddy covariance data. *Scientific Data* **7**, 225, doi:10.1038/s41597-020-0534-3 (2020).

25 McNaughton, K. G. & Jarvis, P. G. Predicting effects of vegetation changes on transpiration and evaporation. *Water deficits and plant growth* **7**, 1-47 (1983).

26 Raupach, M. R. Combination theory and equilibrium evaporation. *Quarterly Journal of the Royal Meteorological Society* **127**, 1149-1181, doi:10.1002/qj.49712757402 (2001).

27 McColl, K. A. & Rigden, A. J. Emergent simplicity of continental evapotranspiration. *Geophysical Research Letters* **n/a**, e2020GL087101, doi:10.1029/2020gl087101 (2020).

28 Gentine, P., Entekhabi, D. & Polcher, J. The Diurnal Behavior of Evaporative Fraction in the Soil–Vegetation–Atmospheric Boundary Layer Continuum. *Journal of Hydrometeorology* **12**, 1530-1546, doi:10.1175/2011jhm1261.1 (2011).

29 Gentine, P., Entekhabi, D., Chehbouni, A., Boulet, G. & Duchemin, B. Analysis of evaporative fraction diurnal behaviour. *Agricultural and Forest Meteorology* **143**, 13-29, doi:10.1016/j.agrformet.2006.11.002 (2007).

30 Byrne, M. P. & O'Gorman, P. A. Trends in continental temperature and humidity directly linked to ocean warming. *Proceedings of the National Academy of Sciences* **115**, 4863-4868, doi:10.1073/pnas.1722312115 (2018).

31 Bouchet, R. J. Evapotranspiration réelle et potentielle, signification climatique. *IAHS Publ* **62**, 134-142 (1963).

32 Fisher, J. B., Tu, K. P. & Baldocchi, D. D. Global estimates of the land–atmosphere water flux based on monthly AVHRR and ISLSCP-II data, validated at 16 FLUXNET sites. *Remote Sensing of Environment* **112**, 901-919, doi:10.1016/j.rse.2007.06.025 (2008).

33 Knauer, J., El-Madany, T. S., Zaehle, S. & Migliavacca, M. Bigleaf—An R package for the calculation of physical and physiological ecosystem properties from eddy covariance data. *PLOS ONE* **13**, e0201114, doi:10.1371/journal.pone.0201114 (2018).

34 Thom, A. S. Momentum, mass and heat exchange of vegetation. *Quarterly Journal of the Royal Meteorological Society* **98**, 124-134, doi:10.1002/qj.49709841510 (1972).

35 Wilson, K. *et al.* Energy balance closure at FLUXNET sites. *Agricultural and Forest Meteorology* **113**, 223-243, doi:10.1016/S0168-1923(02)00109-0 (2002).

36 Morillas, L., Hund, S. V. & Johnson, M. S. Water Use Dynamics in Double Cropping of Rainfed Upland Rice and Irrigated Melons Produced Under Drought-Prone Tropical Conditions. *Water Resources Research* **0**, doi:10.1029/2018wr023757 (2019).

37 Baldocchi, D. *et al.* FLUXNET: A new tool to study the temporal and spatial variability of ecosystem-scale carbon dioxide, water vapor, and energy flux densities. *Bulletin of the American Meteorological Society* **82**, 2415-2434, doi:10.1175/1520-0477(2001)082<2415:FANTTS>2.3.CO;2 (2001).

38 Marsh, A. *Psychrometric Chart*, <https://drajmarsh.bitbucket.io/psychro-chart2d.html> (2018).

Figures:

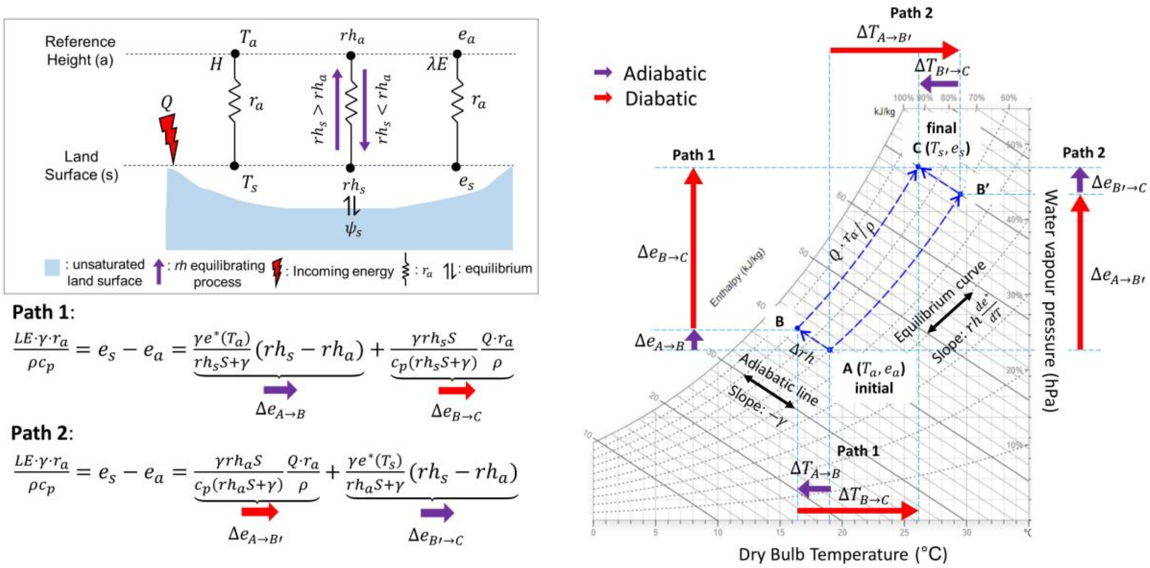

Fig. 1. Schematic conceptualization of the PM_{rh} model and psychrometric relationship of PM_{rh}. The psychrometric chart is modified from Marsh [38]. Path 1 represents Eq. (2) divided by $\frac{\rho c_p}{\gamma r_a}$ while Path 2 represents Eq. (3) divided by $\frac{\rho c_p}{\gamma r_a}$. Here, the enthalpy change of the air parcel is defined as $\frac{Q\cdot r_a}{\rho}$ (kJ kg^{-1}).

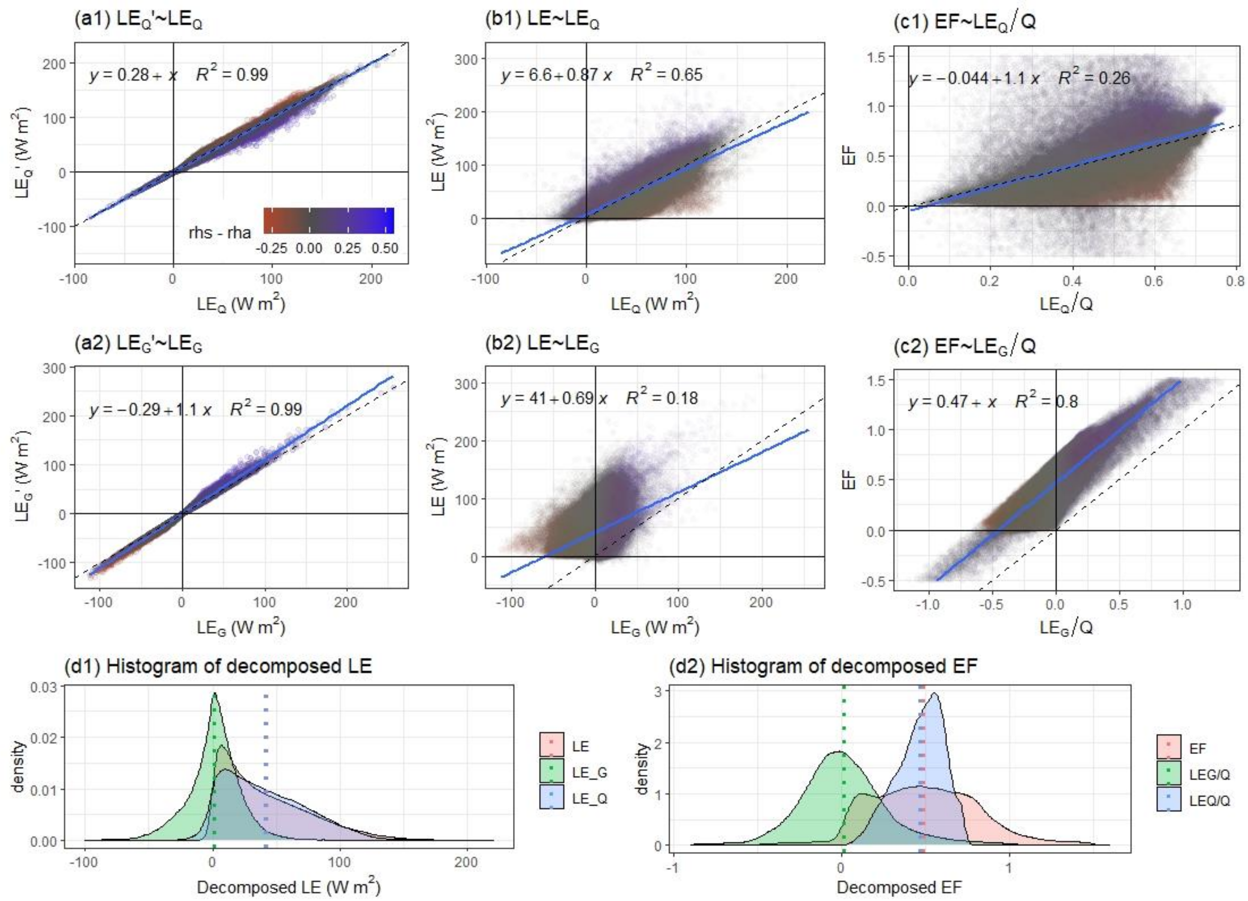

Fig. 2. FLUXNET2015 [24] daily *LE*, LE_Q, and LE_G for 212 sites and 1532 site-years. Panels (a1) and (a2) are linear regressions of LE_Q' on LE_Q and LE_G' on LE_G. Panels (b1) and (b2) are linear regressions of *LE* on LE_Q and *LE* on LE_G. Panels (c1) and (c2) are linear regressions of EF on LE_Q/Q and *EF* on LE_G/Q. In these panels, daily EF data within a range from -1 to 1.5 are only shown. Here, dashed lines are one-to-one lines, blue lines are regression lines, and color represents rh_s−rh_a. Panel (d1) and (d2) are histograms of decomposed *LE* and EF with mean values (dotted lines). To correct for lack of energy balance closure, in all calculations *Q* was set equal to *LE*+*H*.

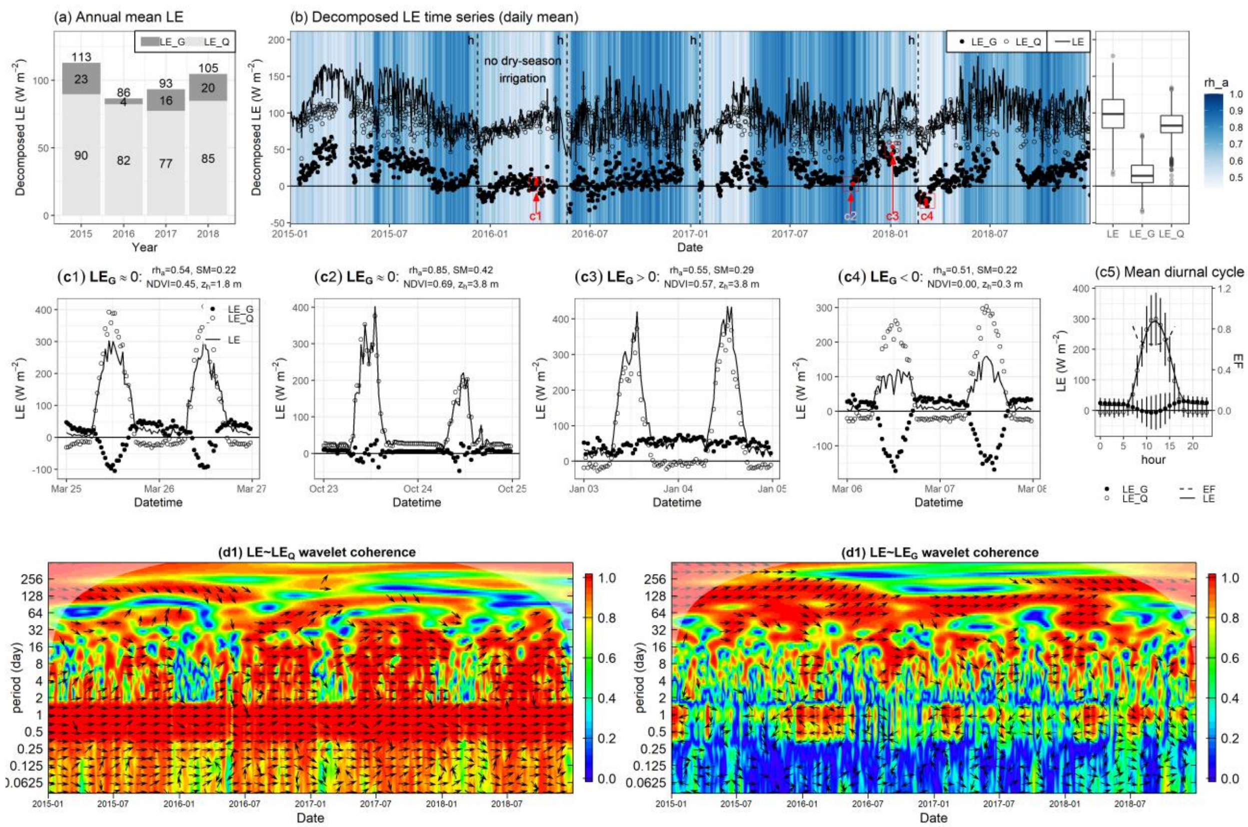

Fig. 3. Time series of LE, LE_Q, and LE_G for the sugarcane eddy-covariance tower site in Costa Rica. Panel (a) is mean annual LE and its components and (b) is a time series of daily mean values with a background color of rh_a. Dashed lines with "h" in panel (b) indicate sugarcane harvest. Panels (c1) ~ (c4) are half-hourly time series indicated in panel (b). Here, SM is volumetric soil water content, NDVI is normalized difference vegetation index, and z_h is canopy height. Panel (c5) presents the long-term mean diurnal cycle of decomposed LE and EF. Panels (d1) and (d2) are wavelet coherence of LE with LE_Q and LE with LE_G. Red and blue colors indicate high and low correlation, respectively. Arrows (pointing right: in-phase; left: antiphase) only appear when the coherence is significant ($p<0.01$).

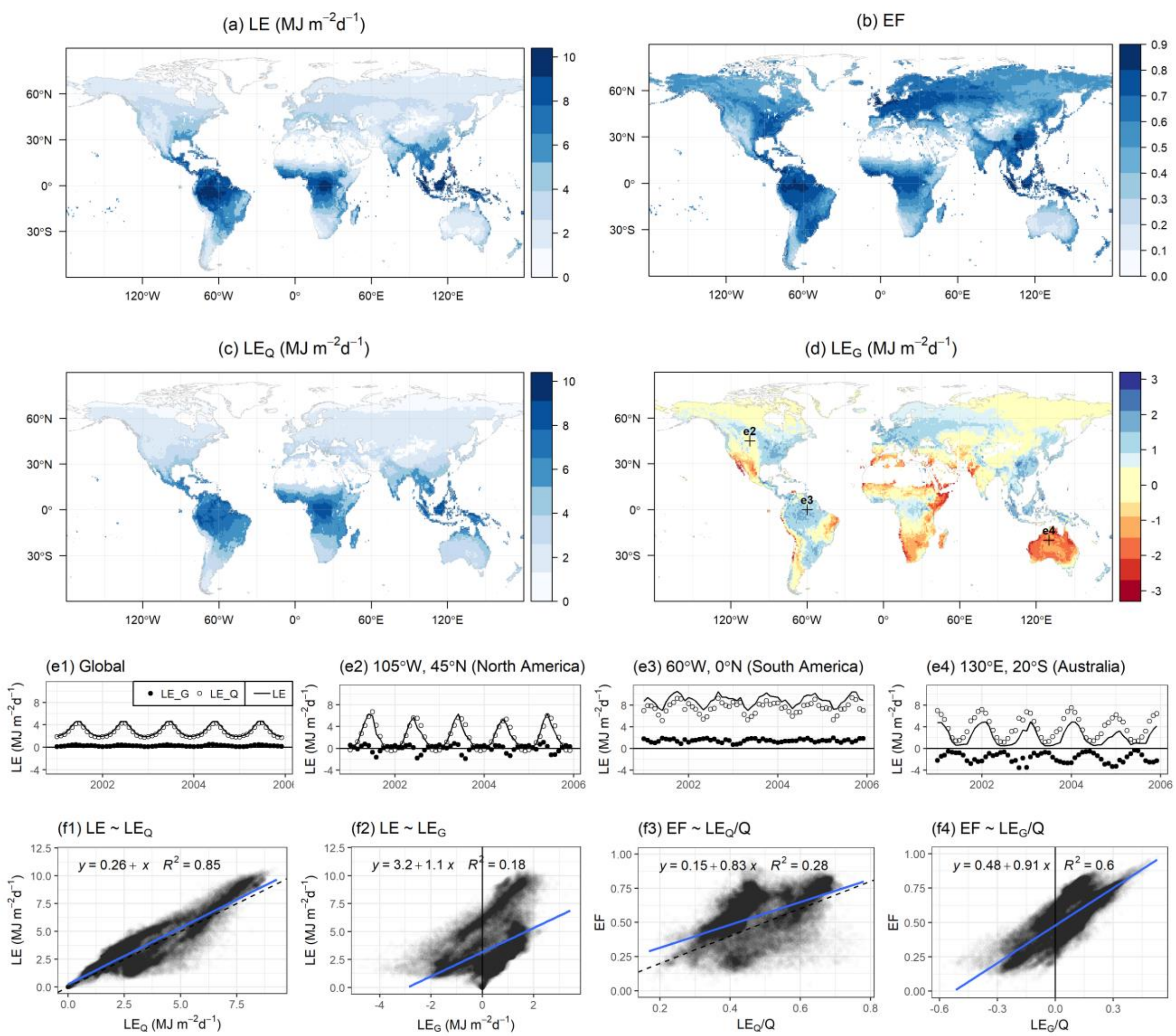

Fig. 4. Mean annual *LE*, EF, LE_Q, and LE_G from 2001 to 2005 (panels (a), (b), (c), and (d), respectively). Panel (e1) is a time series of monthly global average *LE* and the two components, *LE* and LE_Q. Panels (e2), (e3), and (e4) are time series at specific locations highlighted in panel (d). Panels (f1), (f2), (f3), and (f4) are spatial linear regressions of *LE* on LE_Q, *LE* on LE_G, EF on LE_Q/Q, and EF on LE_G/Q, respectively.

Supplemental Information for

Relative humidity gradients as a key constraint on terrestrial water and energy fluxes

Authors: Yeonuk Kim*, Monica Garcia, Laura Morillas, Ulrich Weber, T. Andrew Black, Mark S. Johnson

*Correspondence to: yeonuk.kim.may@gmail.com

Appendix A: Two forms of PM_{rh}

Derivation of Equation (2)

LE and *H* can be written using aerodynamic resistance for water vapour (r_{av}) and sensible heat (r_{aH}) as follows

$$LE = \frac{\rho c_p}{\gamma} \frac{rh_s e^*(T_s) - rh_a e^*(T_a)}{r_{av}} \quad \text{(A1)}$$

$$H = \rho c_p \frac{T_s - T_a}{r_{aH}} \quad \text{(A2)}$$

To express *LE* as a function of T_a and rh_s, adding $-rh_s e^*(T_a) + rh_s e^*(T_a)$ to the numerator of (A1) yields:

$$LE = \frac{\rho c_p}{\gamma} \frac{rh_s e^*(T_s) - rh_s e^*(T_a) + rh_s e^*(T_a) - rh_a e^*(T_a)}{r_{av}} = \frac{\rho c_p}{\gamma} rh_s \frac{e^*(T_s) - e^*(T_a)}{r_{av}} + \frac{\rho c_p}{\gamma} e^*(T_a) \frac{rh_s - rh_a}{r_{av}} \quad \text{(A3)}$$

Next, we use the linearized slope of e^* ($\frac{e^*(T_s) - e^*(T_a)}{T_s - T_a} \approx \frac{de^*}{dT}|_{T=T_a} = S$) to give

$$LE = \frac{\rho c_p}{\gamma} rh_s S \frac{T_s - T_a}{r_{av}} + \frac{\rho c_p}{\gamma} e^*(T_a) \frac{rh_s - rh_a}{r_{av}} \quad \text{(A4)}$$

If we assume $r_{aH} \approx r_{av} \approx r_a$, Eq. (A4) becomes

$$LE = rh_s \frac{S}{\gamma} H + \frac{\rho c_p}{\gamma} e^*(T_a) \frac{rh_s - rh_a}{r_a} \quad \text{(A5)}$$

Then, substituting the surface energy balance ($H = Q - LE$) into the first term of Eq. (A5):

$$LE = \underbrace{\frac{rh_s S}{rh_s S + \gamma} Q}_{Diabatic} + \underbrace{\frac{\rho c_p \, e^*(T_a)}{rh_s S + \gamma} \frac{rh_s - rh_a}{r_a}}_{Adiabatic} \quad \text{(A6)}$$

Derivation of Equation (3)

LE and *H* can be written using aerodynamic resistance for water vapour (r_{av}) and sensible heat (r_{aH}) as follows

$$LE = \frac{\rho c_p}{\gamma} \frac{rh_s e^*(T_s) - rh_a e^*(T_a)}{r_{av}} \quad \text{(A\#7)}$$

$$H = \rho c_p \frac{T_s - T_a}{r_{aH}} \quad \text{(A\#8)}$$

To express *LE* as a function of T_s and rh_a, adding $-rh_a e^*(T_s) + rh_a e^*(T_s)$ to the numerator of (A#1) yields:

$$LE = \frac{\rho c_p}{\gamma} \frac{rh_s e^*(T_s) - rh_a e^*(T_s) + rh_a e^*(T_s) - rh_a e^*(T_a)}{r_{av}} = \frac{\rho c_p}{\gamma} e^*(T_s) \frac{rh_s - rh_a}{r_{av}} + \frac{\rho c_p}{\gamma} rh_a \frac{e^*(T_s) - e^*(T_a)}{r_{av}} \quad \text{(A\#9)}$$

Next, we use the linearized slope of e^* ($\frac{e^*(T_s) - e^*(T_a)}{T_s - T_a} \approx \frac{de^*}{dT}|_{T=T_a} = S$) to give

$$LE = \frac{\rho c_p}{\gamma} e^*(T_s) \frac{rh_s - rh_a}{r_{av}} + \frac{\rho c_p}{\gamma} rh_a S \frac{T_s - T_a}{r_{av}} \quad \text{(A\#10)}$$

If we assume $r_{aH} \approx r_{av} \approx r_a$, Eq. (A#4) becomes

$$LE = \frac{\rho c_p}{\gamma} e^*(T_s) \frac{rh_s - rh_a}{r_a} + rh_a \frac{S}{\gamma} H \quad \text{(A\#11)}$$

Then, substituting the surface energy balance ($H = Q - LE$) into the second term of Eq. (A#5):

$$LE = \underbrace{\frac{\rho c_p \, e^*(T_s)}{rh_a S + \gamma} \frac{rh_s - rh_a}{r_a}}_{Adiabatic} + \underbrace{\frac{rh_a S}{rh_a S + \gamma} Q}_{Diabatic} \quad \text{(A\#12)}$$

Appendix B: Detailed data processing

FLUXNET2015. We only included daily FLUXNET2015 data [1] for periods for which the quality control (QC) flag indicated more than 80 % half-hourly data were present (i.e., measured data in general, or good quality gap-filled data in cases of partially missing data). Detailed description on QC flag can be found in Pastorello, et al. [1].

The sum of *LE* and *H* measured by eddy-covariance system is typically lower than the difference between net radiation (R_n) and the soil heat flux (*G*), resulting in a known condition referred to as the surface energy imbalance (e.g., energy balance closure problem) [2,3]. In order to apply the PM_{rh} model, energy balance closure should be assumed. To generate Figure 2, we attributed the energy imbalance to unmeasured heat storage term, which means that *Q* was defined as *LE+H*. We also investigated the impact of "forcing" energy balance closure by setting $LE + H$ equal to $Rn - G$ and weighting *LE* and *H* based on the assumption that the Bowen ratio ($B = H/LE$) is correct [1]. This resulted in Figure S1, which shows almost identical results as those presented in Figure 2.

In-situ dataset. The sugar cane eddy-covariance tower site has a wet-dry tropical climate, with median monthly air temperature ranging from 27 °C to 30 °C at the nearest climate station in Santa Cruz, 25 km away from our study site, from 1996 to 2018. The dry season lasts from December to March (7 mm/month on average at the climate station in Santa Cruz) and the wet season from April to November (203 mm/month at the climate station in Santa Cruz). The Province of Guanacaste experienced drought in 2015 [4], the first year of eddy-covariance observational data (1127 mm/year in 2015 at the study plot vs. 1652 mm/year long-term average at the climate station).

A ratooning practice is applied in growing sugarcane, a perennial plant. Ratooning means cutting most of the above-ground portion when harvesting the crop, but leaving the roots intact to allow the sugarcane to regrow from the established roots. This ratooning is conducted once a year at the study site. About 5 years after initial planting, regrowth becomes less vigorous and new sugarcane plants are planted. In the middle of 2016, a new planting was started in the flux tower footprint area. The growing season length at the site is about a year, but it varies with regrowth times after the initial planting. Therefore, harvest timing varied from December to May during the study period (Fig. 3 (b)). Crop canopy height varied from 0.01 m to 3.8 m above ground during each harvest cycle. Sugarcane was watered in the dry season via furrow irrigation events, with the exception of 2016 when there was no irrigation due to the replanting.

An eddy-covariance (EC) flux tower was installed 6 m above ground inside a sugarcane plot. The study plot is located in a homogenous landscape where about 200 km^2 around study site is devoted to sugarcane agriculture. The EC system included an open-path infrared gas analyzer (LI-7500A, LI-COR Biosciences, Lincoln, NE, USA) and a sonic anemometer (model 81000, R.M. Young, Traverse City, MI, USA). A soil heat flux plate (HFP01SC-L, Campbell Scientific, Logan, UT, USA) was installed 8 cm below ground, and two net radiometers (2015-2016: NR-LITE, Campbell Scientific, Logan, UT, USA; 2017-2018: SN-500, Apogee Instruments, Logan, UT, USA) were sequentially installed at 5.7 m height. For complementary meteorological measurements, two Vaisala WXT520 weather transmitters (Vaisala Inc. Helsinki, Finland) were installed at 3.6 m and 1.6 m heights. The 1.6 m height Vaisala transmitter was installed within the canopy next to the tower while the 3.6 m height Vaisala weather transmitter located about 25 m from the EC tower but sharing the same patch with the EC system. The volumetric soil water content and soil temperature were measured at several depths at the site

(GS3, Decagon Devices, Pullman, WA, USA); here we report only values at the 8 cm depth. Normalized difference vegetation index (NDVI) was also measured by proximal tower-mounted sensors (SRS, Decagon Devices) beginning in 2017. NDVI values presented for context in Fig. 3 (c2), (c3), and (c4) were measured at the tower, while the NDVI value in Fig. 3 (c1) was retrieved from Landsat7 as that time interval preceded installation of the proximal NDVI sensor.

High frequency raw EC data were processed, and block averaged with EddyPro software (versions 6.0.0 to 6.2.1, LI-COR Biosciences, Lincoln, NE, USA). The processes includes double rotation coordinate correction [5], frequency response correction [6], and density correction [7]. Block averaged fluxes at 30-min intervals went through a quality control procedure from which fluxes were removed when any of the following conditions occurred, following Morillas, et al. [4]: periods of heavy rain, low signal strength (signal strength < 60%), measurements flagged as low quality by the EddyPro software, or during conditions with low friction velocity (u_*) based on moving point method [8,9]. Subsequently, the resulting gaps in 30-min turbulent fluxes were gap-filled using the marginal distribution sampling method [9,10].

Vapour pressure (e_a) measured by the open-path infrared gas analyzer (IRGA) was used to calculate rh_a. To ensure data quality of e_a, data were also filtered out when any of the following conditions occurred: periods of heavy rain, low signal strength (signal strength <60%), measurements flagged as low quality by the EddyPro software, and unrealistic values recorded by the IRGA compared to Vaisala measurements (more than 20% difference when calculating relative humidity). The resulting IRGA gaps in the e_a time series were replaced by the corresponding measurements made using the Vaisala sensor at the 3.6 m height.

For the study period, the surface energy balance closure of 30 min data was 86 %, which is typical of high-quality eddy-covariance data sets [2]. When canopy height was less than 1 m, the surface energy balance was almost closed (97%), whereas the closure was 83 % when canopy height was higher than 1 m. Considering a possible significant role of unmeasured canopy and soil heat storages [11,12] and the homogenous landscape of the study site [3,13], we did not force the energy closure. Therefore, for PM_{rh} application, we defined Q as a sum of LE and H instead of the difference between net radiation and soil heat flux by attributing the cause of the surface energy imbalance to unmeasured heat storage terms following Moon, et al. [14].

In order to explore the time scale of the covariances for $LE \sim LE_Q$ and $LE \sim LE_G$ in the frequency domain, we applied wavelet coherence analysis using WaveletComp R package [15]. The package is designed to apply the continuous wavelet transform using Morlet wavelet, which is a popular approach to analyze hydrological and micrometeorological datasets [16,17]. A total time series of half-hourly decomposed LE for the 4-year measurement period was used to estimate localized coherence and phase angle. The wavelet coherence can be interpreted as the local correlation between two variables in the frequency-time domain (see Fig. 3, where red indicates high correlation). 0° phase angle (arrow pointing right) indicates periods of positive correlation while 180° phase angle (arrow pointing left) indicates periods of negative correlation.

References:

1 Pastorello, G. *et al.* The FLUXNET2015 dataset and the ONEFlux processing pipeline for eddy covariance data. *Scientific Data* **7**, 225, doi:10.1038/s41597-020-0534-3 (2020).

2 Wilson, K. *et al.* Energy balance closure at FLUXNET sites. *Agricultural and Forest Meteorology* **113**, 223-243, doi:10.1016/S0168-1923(02)00109-0 (2002).

3 Stoy, P. C. *et al.* A data-driven analysis of energy balance closure across FLUXNET research sites: The role of landscape scale heterogeneity. *Agricultural and Forest Meteorology* **171-172**, 137-152, doi:10.1016/j.agrformet.2012.11.004 (2013).

4 Morillas, L., Hund, S. V. & Johnson, M. S. Water Use Dynamics in Double Cropping of Rainfed Upland Rice and Irrigated Melons Produced Under Drought-Prone Tropical Conditions. *Water Resources Research* **0**, doi:10.1029/2018wr023757 (2019).

5 Wilczak, J. M., Oncley, S. P. & Stage, S. A. Sonic Anemometer Tilt Correction Algorithms. *Boundary-Layer Meteorology* **99**, 127-150, doi:10.1023/A:1018966204465 (2001).

6 Moncrieff, J. B. *et al.* A system to measure surface fluxes of momentum, sensible heat, water vapour and carbon dioxide. *Journal of Hydrology* **188-189**, 589-611, doi:10.1016/S0022-1694(96)03194-0 (1997).

7 Webb, E., Pearman, G. & Leuning, R. Correction of flux measurements for density effects due to heat and water vapour transfer. *Quarterly Journal of the Royal Meteorological Society* **106**, 85-100 (1980).

8 Papale, D. *et al.* Towards a standardized processing of Net Ecosystem Exchange measured with eddy covariance technique: algorithms and uncertainty estimation. *Biogeosciences* **3**, 571-583, doi:10.5194/bg-3-571-2006 (2006).

9 Wutzler, T. *et al.* Basic and extensible post-processing of eddy covariance flux data with REddyProc. *Biogeosciences Discussions*, doi:10.5194/bg-15-5015-2018 (2018).

10 Reichstein, M. *et al.* On the separation of net ecosystem exchange into assimilation and ecosystem respiration: review and improved algorithm. *Global Change Biology* **11**, 1424-1439, doi:10.1111/j.1365-2486.2005.001002.x (2005).

11 Leuning, R., van Gorsel, E., Massman, W. J. & Isaac, P. R. Reflections on the surface energy imbalance problem. *Agricultural and Forest Meteorology* **156**, 65-74, doi:10.1016/j.agrformet.2011.12.002 (2012).

12 Eshonkulov, R., Poyda, A., Ingwersen, J., Pulatov, A. & Streck, T. Improving the energy balance closure over a winter wheat field by accounting for minor storage terms. *Agricultural and Forest Meteorology* **264**, 283-296, doi:10.1016/j.agrformet.2018.10.012 (2019).

13 Foken, T. The energy balance closure problem: an overview. *Ecological Applications* **18**, 1351-1367, doi:10.1890/06-0922.1 (2008).

14 Moon, M., Li, D., Liao, W., Rigden, A. J. & Friedl, M. A. Modification of surface energy balance during springtime: The relative importance of biophysical and meteorological changes. *Agricultural and Forest Meteorology* **284**, 107905, doi:10.1016/j.agrformet.2020.107905 (2020).

15 Roesch, A. & Schmidbauer, H. WaveletComp: Computational Wavelet Analysis. (2014).

16 Hatala, J. A., Detto, M. & Baldocchi, D. D. Gross ecosystem photosynthesis causes a diurnal pattern in methane emission from rice. *Geophysical Research Letters* **39**, 1-5, doi:10.1029/2012GL051303 (2012).

17 Johnson, M. S. *et al.* Soil CO2 Dynamics in a Tree Island Soil of the Pantanal: The Role of Soil Water Potential. *PLOS ONE* **8**, e64874, doi:10.1371/journal.pone.0064874 (2013).

5

Supplement Figures:

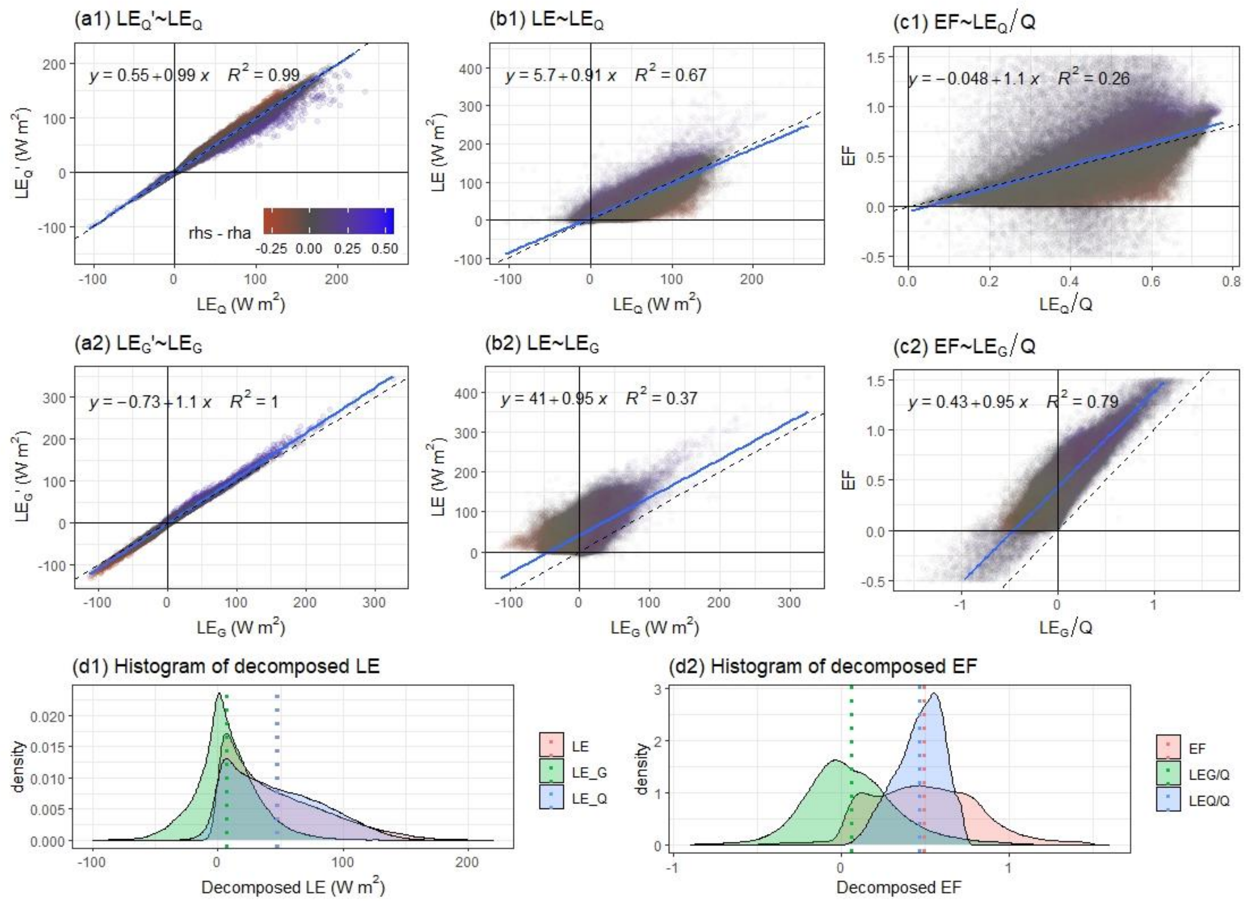

Figure S1. FLUXNET2015 [1] daily *LE*, LE_Q, and LE_G (energy balance corrected). Panels (a1) and (a2) are linear regressions of LE_Q' on LE_Q and LE_G' on LE_G. Panels (b1) and (b2) are linear regressions of *LE* on LE_Q and *LE* on LE_G. Panels (c1) and (c2) are linear regressions of EF on LE_Q/Q and *LE* on LE_G/Q. Here, dashed lines are one-to-one lines, blue lines are regression lines, and color represent rh_s-rh_a. Panel (d1) and (d2) are histograms of decomposed *LE* and EF with mean values (dotted line).